Supplementary Information for

Refining the band structure of BiOBr nanosheets through the synergetic effects of VO_4^{3-} ions replacement and oxygen vacancies for the promoted visible-light-driven photocatalysis

Lulu Wang, Changming Zhao, Zhengrong Xiang, Yi Zhang, Nan Ma, Jie shen, Xiahui Peng, Shiying Zhang, Zhongfu Li, Zhaohui Wu

Table of Contents

1. Tables

Table S1. General experimental conditions and resulted phase of final products.

No.	BiOBr (mmol)	NH_4VO_3 (mmol)	NH_4VO_3/BiOBr	Phase of products
1	1	0.05	0.05	BiOBr
2	1	0.1	0.1	BiOBr/$BiVO_4$
3	1	0.5	0.5	BiOBr/$BiVO_4$
4	1	1	1	BiOBr/$BiVO_4$/$BiV_{1.025}O_{4+x}$
5	1	2	2	$BiVO_4$/$BiV_{1.025}O_{4+x}$
6	1	3	3	$BiVO_4$/$BiV_{1.025}O_{4+x}$

Table S2. ICP results of products obtained by adding 0.05 mmol of VO_3^-

Sample weight（g)	Elements	Amount of element in solution（mg/L)	Percentage of element（%)
0.0451	Bi	3.39	75.21%
0.0451	V	0.70	1.56%

Table S3. Parameters of band structure of BiOBr without and with oxygen vacancy, and BiOBr with oxygen vacancies and VO_4^{3-} ions replacement.

	BiOBr	BiOBr (V_O)	BiOBr (V_O + VO_3^- ions replacement)
Cell parameters	a = 7.875504 Å, b = 7.875504 Å, c = 8.146860 Å, α = β = γ = 90°	a = 7.873221Å, b = 7.873221 Å, c = 8.257360 Å, α = β = γ = 90°	a = 8.165413 Å, b = 7.947960 Å, c = 8.449130 °, α = 90.091141°, β = 90.823715°, γ = 90.161331°
bandgap (E_g, eV)	2.155	2.483	2.403

2. Results and discussions

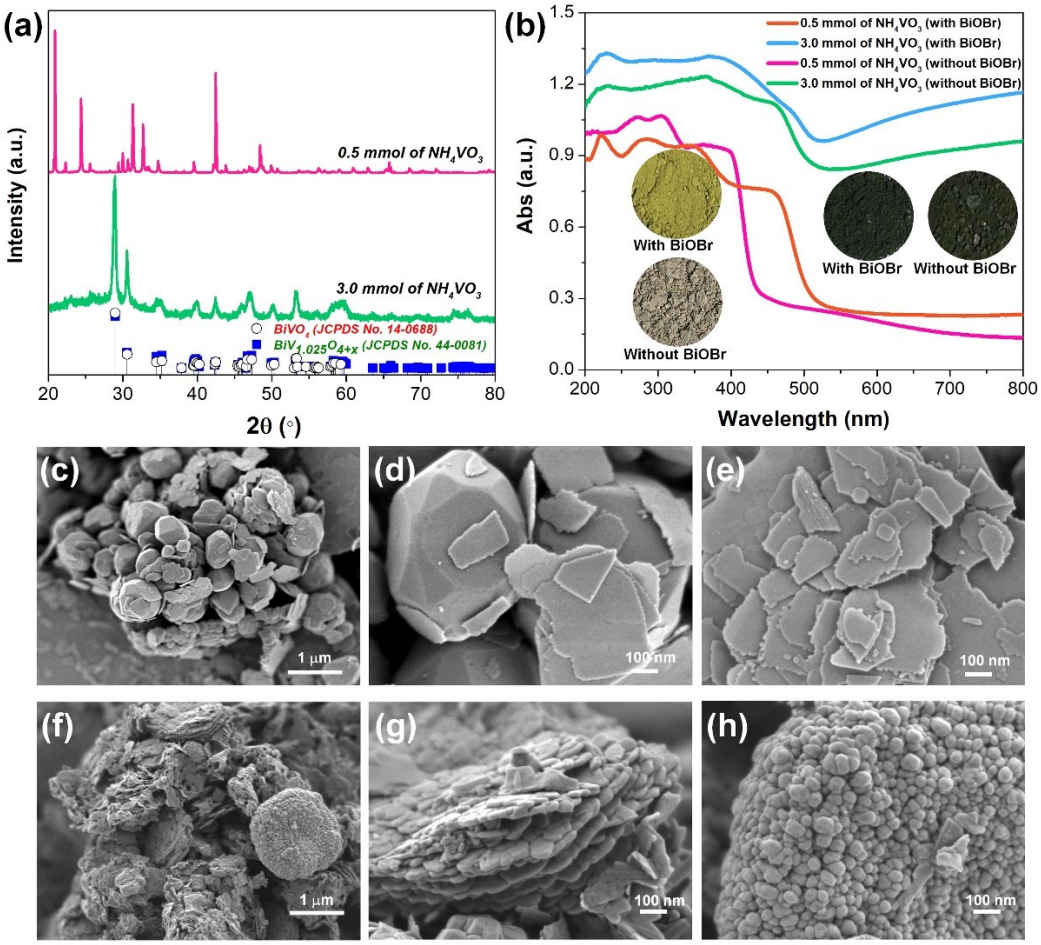

Fig. S1. (a) XRD pattens, (b) DRS spectra and corresponding photographs of products obtained at different concentration of NH_4VO_3 but without BiOBr. (c), (d) and (e) were SEM images of products obtained at 0.5 mmol of NH_4VO_3 but without BiOBr, (f), (g) and (h) were SEM images of products obtained at 3.0 mmol of NH_4VO_3 but without BiOBr.

Altering the concentration of NH_4VO_3 but without BiOBr nanosheets as templates, the resulted XRD patterns were recorded (**Fig. S1**). Apparently, the products obtained by adding 0.5 mmol of NH_4VO_3 were not indexed to $BiVO_4$ because the excessive $Bi(NO_3)_3{\cdot}5H_2O$ hindered the formation of $BiVO_4$. While, increasing the concentration of NH_4VO_3 to 3.0 mmol, the characteristic peaks of resulted products were assigned to $BiVO_4$ (JCPDS No. 14-0688) and $BiV_{1.025}O_{4+x}$ (JCPDS No. 44-0081). Accordingly, the

45 products obtained by adding 0.5 mmol of NH_4VO_3 only exhibited absorbance edge of
46 ~450 nm due to the absence of $BiVO_4$ (**Fig. S1b**). While, with and without BiOBr, the
47 products obtained by adding 3.0 mmol of NH_4VO_3 showed similar optical absorbance
48 region covering the whole violet and visible light region owing to the presence of
49 $BiV_{1.025}O_{4+x}$. The morphology of products produced by adding 0.5 mmol of NH_4VO_3
50 were mixed with nanosheets and irregular polyhedron (**Fig. S1c** to **S1e**).
51 Comparatively, the products resulted by adding 3.0 mmol of NH_4VO_3 were stacked
52 with assembled sheets and assembled particles (**Fig. S1f** to **S1h**).

53 The Raman shifts reflect the structure variation of different samples (**Fig. S2**).
54 According to the dimensionless intensity of different products (**Fig. S2a**), the vibration
55 and stretching mode assigned to BiOBr and $BiVO_4$ were evolved gradually, when
56 increasing the concentration of VO_3^-. Furthermore, when increasing the concentration
57 of VO_3^-, the Raman intensity of different products increased firstly (until 0.5 mmol of
58 VO_3^-), and then diminished subsequently (from 0.5 to 3.0 mmol). This change of
59 Raman intensity suggested that the vibrations and stretches of BiOBr and $BiVO_4$ were
60 weakening. As examined the local magnified Raman spectra, the shifts of different
61 bonds were exploited. For the BiOBr nanosheets, strong peaks of 92.8 and 112.8 cm^{-1}
62 ascribed to the A_{1g} first-order vibration modes of Bi-metal and A_{1g} internal Bi-Br
63 stretching mode, respectively.[1, 2] While, a weak peak located at 161.4 cm^{-1} assigned to
64 the E_g Bi-Br stretching mode (**Fig. S2b**). When increasing the concentration of VO_3^-,
65 the A_{1g} vibration mode of Bi-metal and E_g Bi-Br stretching mode were gradually
66 depleted and diminished (**Fig. S2c**). When increasing the concentration of VO_3^- over
67 0.1 mmol, the peaks located at 210.8, 321.6, 368.1, and 829.1 cm^{-1} assigned to $BiVO_4$
68 were observed (**Fig. S2d-e**).[3, 4] Particularly, Raman shifts of 321.6 and 368.1 ascribed
69 to the asymmetric and symmetric bending modes of the VO_4^{3-} tetrahedra units could

be observed (**Fig S2d**). Raman peak of 829.1 cm^{-1} attributed to the V–O bond and 210.8 cm^{-1} produced by the $BiVO_4$ external vibration modes were also present (**Fig S2d** and **S2e**). Notably, the Raman shifts assigned to $BiVO_4$ were red-shifting gradually, indicating that the phonon energy was decreased probably due to structure distortion caused by the VO_4^{3-} ion exchange.[5]

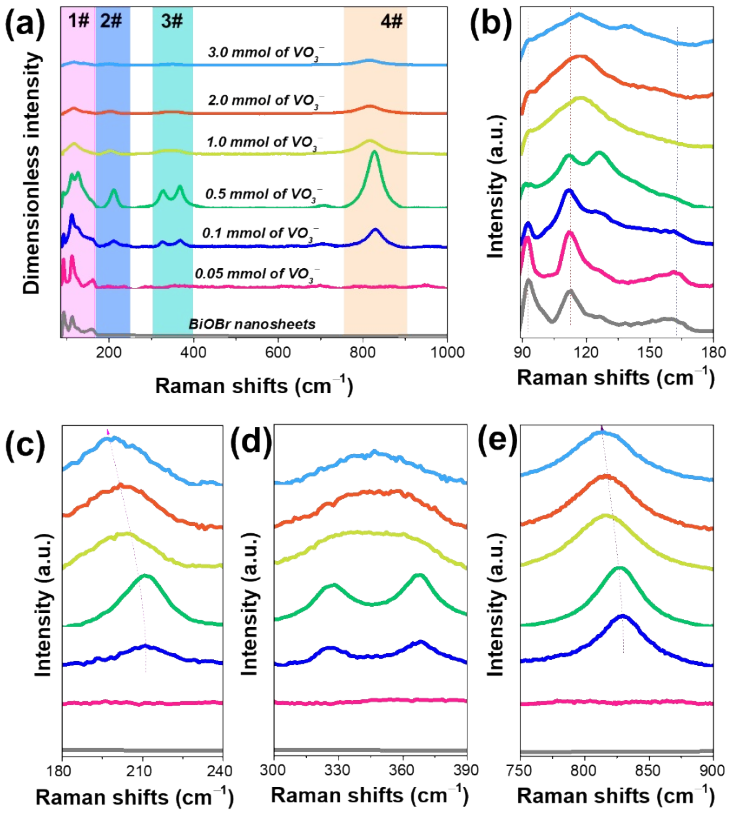

Fig. S2. (a) Raman shifts, local magnified Raman shifts of different marked numbers, (b) 1#, (c) 2#, (d) 3#, and (e) 4#.

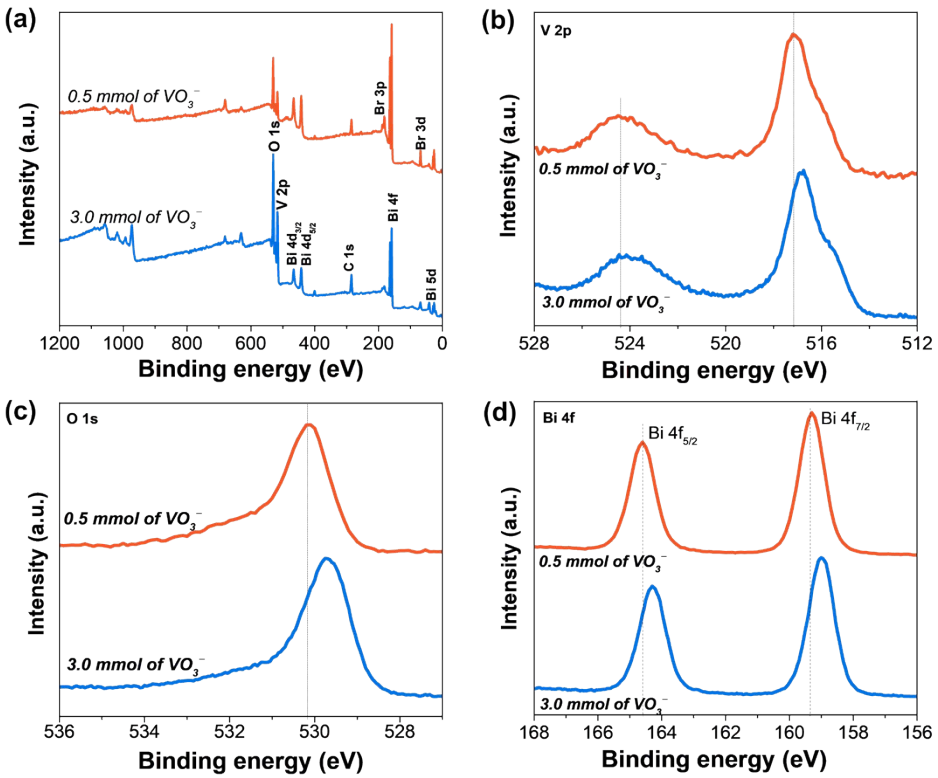

Fig. S3. (a) XPS survey spectra, high-resolution XPS spectra of (b) V 2p, (c) O1s, and (d) Bi 4f of products obtained by adding 0.5 and 3.0 mmol of VO_3^-.

According to survey spectra of products obtained by adding 0.5 and 3.0 mmol of VO_3^-, the concentration of V 2p was continuously increased when increasing the concentration of VO_3^- (**Fig. S3a**). The binding energies located at 524.5 and 517.2 eV respective ascribed to V $2p_{1/2}$ and V $2p_{3/2}$ for products obtained by adding 0.5 mmol of VO_3^- [6], which were shifted to lower binding energies for products by adding 3.0 mmol of VO_3^- (**Fig. S3b**). Accordingly, the Bi–O band, Bi $4f_{5/2}$ and Bi $4f_{7/2}$ binding energies for products obtained by adding 3.0 mmol of VO_3^- were also shifted to lower binding energies (**Fig. S3c** and **S3d**), indicating that the electronegativity of Bi and O increased due to the excessive VO_4^{3-} units, compared with products obtained by adding 0.5 mmol of VO_3^-.[7]

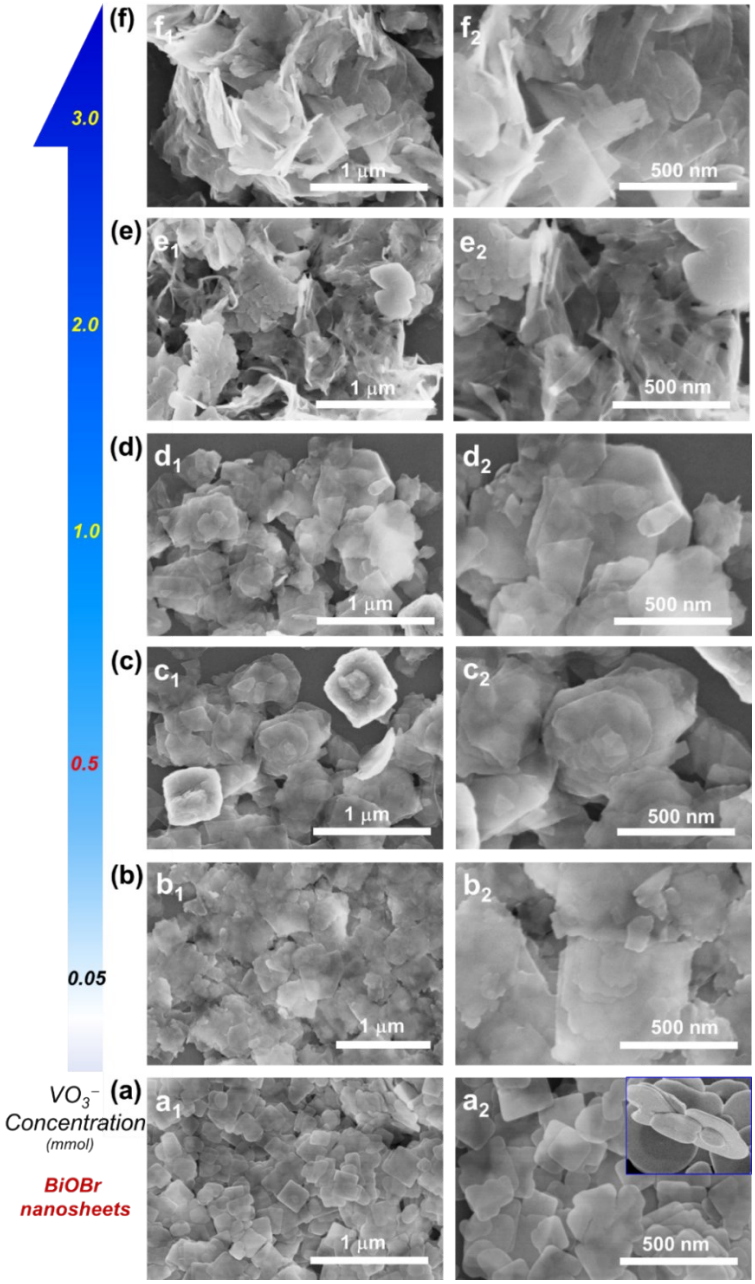

Fig. S4. SEM images of different products generated by adding different concentration of VO_3^-, (a) BiOBr nanosheets, (b) 0.05, (c) 0.5, (d) 1.0, (e) 2.0, (f) 3.0 mmol of VO_3^- (a_1, b_1, c_1, d_1, e_1 and f_1 were the low magnification SEM images of products, a_2, b_2, c_2, d_2, e_2 and f_2 were the high magnification SEM images).

The initial BiOBr showed irregular square sheet-like morphology, and the thickness was ~20 nm (**Fig. S4a**). When gradually increasing the concentration of VO_3^-, the sheet-like morphology of products was maintained but showed slightly

difference (**Fig. S4b-f**). Some nanosheets were broke into small pieces, while some nanosheets were grew up with jagged edges by adding 0.05 mmol of VO_3^- (**Fig. S4b**). When elevating the concentration of VO_3^- to1.0 mmol, small piece of nanosheets disappeared, and the nanosheets were tended to aggregate (**Fig. S4c** and **S4d**). These aggregated nanosheets continuously shifted to more irregular nanosheets at 3.0 mmol of VO_3^- (**Fig. S4e** and **S4f**).

In terms of the BiOBr nanosheets, the thickness was ~20 nm (**Fig. S5a**). The TEM image confirmed the sheet-like morphology (**Fig. S5b**). And the clear perpendicular interplanar lattice spacing of 0.277 nm assigned to (110) planes of BiOBr were observed (**Fig. S5c**). The products obtained by adding 0.1 mmol of NH_4VO_3 also showed sheet-like morphology (**Fig. S5d**). According to the HRTEM image, clear and perpendicular interplanar lattice spacings of 0.277 nm were observed, which were assigned to the (110) atomic planes of BiOBr (**Fig. S5e**). This result indicated that 0.1 mmol of VO_3^- affected the structure of BiOBr barely due to the lower concentration of VO_3^-, which was confirmed by the EDS results (**Fig. S5f–g**).

The products obtained by adding 0.5 mmol of NH_4VO_3 still maintained sheet-like morphology, and the thickness of the resulted nanosheets was ~16.3 nm to 90.7 nm (**Fig. S5h**). Based on the lateral HRTEM image, clear and continuous interplanar lattice spacing of 0.817 nm assigned to the (001) planes of BiOBr were observed (**Fig. S5i**). Compared to the theoretical value of interplanar lattice spacing of 0.810 nm, this value was slightly expanded, indicating that the VO_3^- ions exchange caused the expansion of crystal lattices of initial BiOBr. Furthermore, the component of V was higher than that of Br in the final products based on the EDS spectrum (**Fig. S5j–k**), suggesting that the percentage of VO_3^- replacing the Br of BiOBr increased.

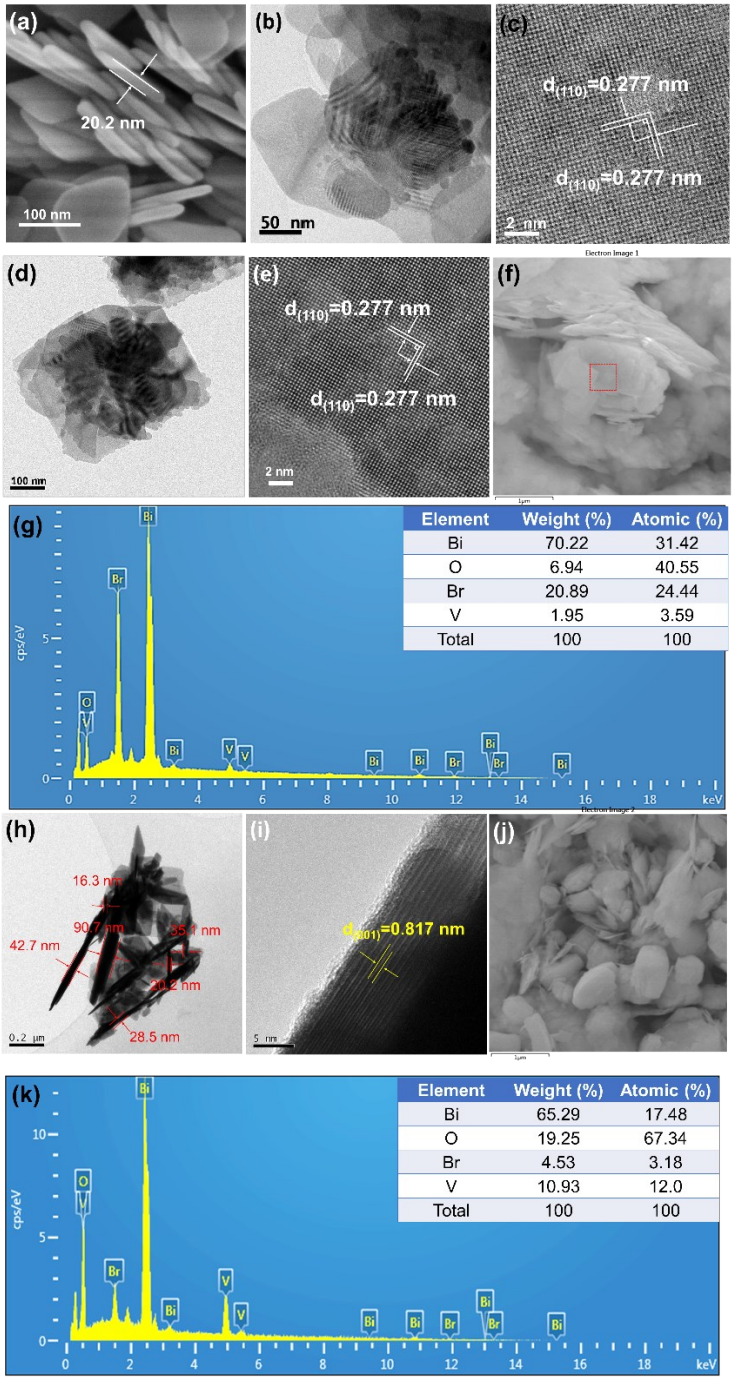

Fig. S5. (a) SEM, (b) TEM and (c) HRTEM images of BiOBr nanosheets. (d) TEM, (e) HRTEM images of products obtained by adding 0.1 mmol of VO_3^-, (f) SEM image and (g) EDS spectrum of the mark in (f) (inset with EDS element percentage). (h) TEM, (i) lateral HRTEM, (j) SEM images, and (k) corresponding elements mapping of products obtained by adding 0.5 mmol of VO_3^-, and EDS spectrum of (j) (inset with EDS element percentage).

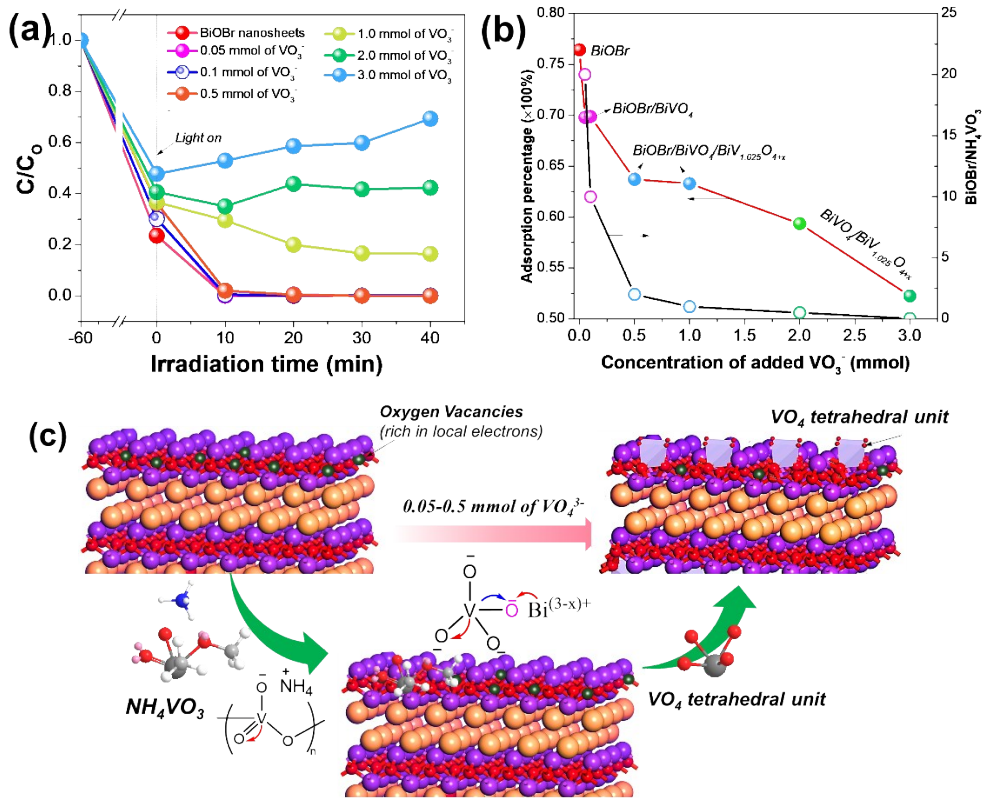

Fig. S6. (a) Photodegradation of RhB over different samples under solar light irradiation, (b) the ratio of BiOBr and NH_4VO_3, the adsorption percentage of RhB and the final phase of products obtained at different concentration of NH_4VO_3. (c) Schematic illustration of oxygen vacancies diminishing and forming VO_4^{3-} tetrahedral unit.

According to previous studies,[8, 9] the native oxygen vacancies possessing massive localized electrons are able to capture positive charge molecules or ions. RhB with positive charge groups of 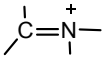 could adsorb onto the surface of BiOBr nanosheets with massive oxygen vacancies. Then, the adsorption efficiency of RhB over BiOBr or $BiOBr/BiVO_4$-based photocatalysts could reflect the variation of surface charge. According to the adsorption efficiency of RhB over different samples (**Fig. S7a**), the RhB adsorption efficiency was gradually decreased when increasing the concentration

of VO_3^-. On the other hand, the templates BiOBr nanosheets was enclosed with (001) facets, which were terminated with $[Bi_2O_2]^{2+}$, which could bond with VO_3^- to form unsaturated VO_4^{3-} tetrahedral units as terminated layer on the surface when slightly increasing the concentration of VO_3^-. These unsaturated VO_4^{3-} tetrahedral units also could contribute to the adsorption of RhB. Thus, the adsorption efficiency of RhB over different products should be the synergetic effect of oxygen vacancies and unsaturated VO_4^{3-} units. At higher concentration of VO_3^- (2 and 3 mmol), final products with phase of $BiVO_4/BiV_{1.025}O_{4+x}$ only with unsaturated VO_4^{3-} units on the surface contributed to the adsorption of RhB (**Fig. S7b**).

The more electronegativity of the O atoms presents in unsaturated V=O bond of VO_3^-, resulting in that the electrophilic properties of V ions. The adjacent bismuth ions of oxygen vacancies are considered as being rich in electrons.[10, 11] The unsaturated V=O is opened and the V bond with the O atoms adjacent to oxygen vacancies on the surface of BiOBr nanosheets due to the nucleophilic reagent of reaction. During this process, the electrons rich in Bi atoms are shifted to the O and transferred to the V to form VO_4^{3-} tetragonal units on the surface of BiOBr nanosheets (**Fig. S7c**).[12] Bi and O adjacent to oxygen vacancies loss the electrons and the bind length of Bi–O bond become longer, when lower concentration of VO_3^- adsorb and interact with the surface of BiOBr with oxygen vacancies. But when the oxygen vacancies are consumed completely and VO_3^- are excessive, the electrons transfer from V to Bi and O, the electronegativity of Bi and O increase, and the Bi–O bond should get shorter.

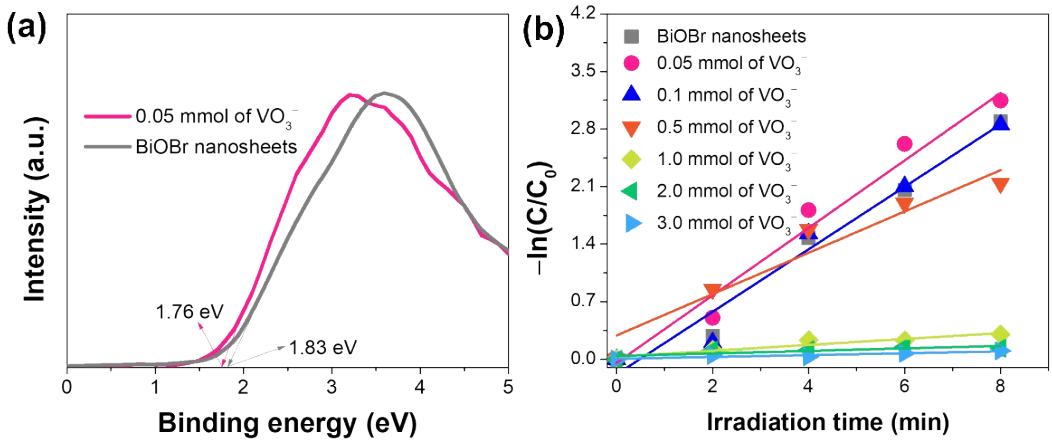

Fig. S7. (a) XPS valence band spectra of BiOBr nanosheets and products obtained by adding 0.05 mmol of VO_3^-. (b) Pseudo first-order kinetic fitting of different samples within 8 min visible-light irradiation.

According to the XPS valence band spectra of BiOBr nanosheets and products obtained by adding 0.05 mmol of VO_3^-, its VB were 1.83 and 1.76 eV, respectively (**Fig. S7a**). Correspondingly, the CB of BiOBr nanosheets and products obtained by adding 0.05 mmol of VO_3^- were –0.99 and –1.03 eV, based on the bandgaps (**Fig. 5**).

The pseudo first-order kinetic fitting of different samples within 8 min visible-light irradiation were plotted and estimated according the equation of $-\ln\left(\frac{C}{C_0}\right) = kt$ (k and t are reaction rate constant and irradiation time, respectively. C and C_0 are the concentration of solution at t and original concentration of solution) (**Fig. S7b**). Apparently, the reaction rate constant of product obtained by adding 0.05 mmol was the superior, while the value of the products obtained at higher concentration of VO_3^- was much lower.

3. References

(1) M. Hu, A. H. Yan, X. Y. Wang, F. Huang, Q. P. Cui, F. Li, J. Huang, Hydrothermal method to prepare Ce-doped BiOBr nanoplates with enhanced carrier transfer and

photocatalytic activity, *Mater. Res. Bull*. **2019**, *116*, 89–97.
(2) H. Wang, D. Y. Yong, S. C. Chen, S. L. Jiang, X. D. Zhang, W. Shao, Q. Zhang, W. S. Yan, B. C. Pan, Y. Xie, Oxygen-vacancy-mediated exciton dissociation in BiOBr for boosting charge-carrier-involved molecular oxygen activation, *J. Am. Chem. Soc.* **2018**, *140*, 1760–1766.
(3) M. Wu, Q. F Jing., X. Y. Feng, L. M. Chen, $BiVO_4$ microstructures with various morphologies: Synthesis and characterization, *Appl. Surf. Sci*. **2018**, *427*, 525–532.
(4) C. J. Shi, X. L. Dong, X. Y. Wang, H. C. Ma, X. F. Zhang, Ag nanoparticles deposited on oxygen-vacancy-containing $BiVO_4$ for enhanced near-infrared photocatalytic activity, *Chinese J. Catal*. **2018**, *39*, 128–137.
(5) N. Aiga, Q. X. Jia, K. Watanabe, A. Kudo, T. Sugimoto, Y. Matsumoto, Electron-phonon coupling dynamics at oxygen evolution sites of visible-light-driven photocatalyst: Bismuth vanadate, *J. Phys. Chem. C* **2013**, *117*, 9881–9886.
(6) Y. P. Zhang, W. B. Li, Z. Y. Sun, Q. Zhang, L. Wang, Z. Y. Chen, In-situ synthesis of heterostructured $BiVO_4$/BiOBr core-shell hierarchical mesoporous spindles with highly enhanced visible-light photocatalytic performance, *J. Alloy Compd*. **2017**, *713*, 78–86.
(7) Q. Wang, Z. Q. Liu, D. M. Liu, W. Wang, Z. W. Zhao, F. Y. Cui, G. B. Li, Oxygen vacancy-rich ultrathin sulfur-doped bismuth oxybromide nanosheet as a highly efficient visible-light responsive photocatalyst for environmental remediation, *Chem. Eng. J.* **2019**, *360*, 838–847.
(8) X. X. Zeng, X. F. Gong, Y. Q. Wan, R. Y. He, Z. D. Xu, Formation of oxygen vacancies on the {010} facets of BiOCl and visible light activity for degradation of ciprofloxacin, *Chem. Res. Chinese U.* **2018**, *34*, 711–718.
(9) H. Li, J. Li, Z. H. Ai, F. L. Jia, L. Z. Zhang, Oxygen vacancy-mediated photocatalysis of BiOCl: Reactivity, selectivity, and perspectives, *Angew. Chem. Int. Ed.* **2018**, *57*, 122–138.
(10) S. J. Wu, J. W. Xiong, J. G. Sun, Z. D. Hood, W. Zeng, Z. Z. Yang, L. Gu, X. X. Zhang, S. Z. Yang, Hydroxyl-dependent evolution of oxygen vacancies enables the regeneration of BiOCl photocatalyst, *ACS Appl. Mater. Inter*. **2017**, *9*, 16620–16626.
(11) X. L. Jin, C. D. Lv, X. Zhou, C. M. Zhang, Q. Q. Meng, Y. Liu, G. Chen, Molecular adsorption promotes carrier migration: Key step for molecular oxygen activation of defective $Bi_4O_5I_2$, *Appl Catal B-Environ.,* **2018**, *226*, 53–60.
(12) J. Q. Yu, A. Kudo, Effects of structural variation on the photocatalytic performance of hydrothermally synthesized $BiVO_4$, *Adv. Funct. Mater*. **2006**, *16*, 2163–2169.